# New Experimental Data of STBLI at DNS/LES Accessible Reynolds Numbers

Patrick Bookey* and Christopher Wyckham†
*Mechanical and Aerospace Engineering, Princeton University, Princeton, NJ 08540*

Alexander Smits‡
*Princeton University, Princeton, NJ 08540*

*and*

M. Pino Martin§
*Princeton University, Princeton, NJ 08540*

**An experimental investigation was conducted to study four shock/turbulent boundary layer interactions. In Mach 2.9 flow, a 24º compression corner and a 12º reflected shock interaction were studied at $Re_\theta$ = 2400. In a Mach 8 flow, an 8º compression corner and a 10º sharp fin were studied at $Re_\theta$ = 3500. These low Reynolds number flows were chosen to coincide with DNS accessible Reynolds numbers in order to make direct comparisons. Measurements included mean flow surveys, surface pressure distributions, surface flow visualizations and Filtered Rayleigh Scattering (FRS). FRS was used to make two-dimensional images of the flow in the streamwise direction giving a qualitative picture of the nature of the interaction. Statistical data of the boundary layer characteristics was also obtained from the FRS images. The results show the incoming boundary layer at both Mach numbers to be fully turbulent. The interactions in Mach 2.9 flow produced large areas of separation. The compression ramp in the Mach 8 flow was found to remain attached throughout the interaction, while the 10º sharp fin produced a large three-dimensional separated region. The preliminary results indicate good agreement between experiment and DNS computations.**

## Nomenclature

| | | |
|---|---|---|
| $M$ | = | Mach number |
| $p$ | = | pressure |
| $C_f$ | = | skin friction coefficient |
| $u$ | = | mean velocity component parallel to flat plate or ramp surface |
| $u_\tau$ | = | friction velocity, $(\tau_w/\rho_w)^{1/2}$ |
| $u+$ | = | Van Driest generalized velocity |
| $\delta$ | = | boundary layer thickness |
| $\delta^*$ | = | displacement thickness, $\delta^* = \int_0^\delta (1 - \rho u / \rho_e u_e)\,dy$ |
| $\delta_0$ | = | incoming boundary layer thickness |
| $\theta$ | = | momentum thickness, $\theta = \int_0^\delta [\rho u / \rho_e u_e](1 - u / u_e)\,dy$ |
| $\tau$ | = | shear stress |

* Student Member AIAA
† Student Member AIAA
‡ Fellow AIAA
§ Member AIAA

$y$ = distance perpendicular to wall of flat plate or ramp
$y+$ = distance perpendicular to wall in wall coordinates
$\alpha$ = angle of fin with respect to freestream
$\beta$ = angle of characteristic features of sharp fin induced surface flow

*Subscripts*
$e$ = boundary layer edge
$w$ = wall
$\infty$ = freestream value, upstream of shock
S = separation

## I. Introduction

MANY aspects of shock/turbulence interactions are not fully understood, including the dynamics of shock unsteadiness; turbulence amplification and mean flow modification induced by shock distortion; separation and reattachment criteria as well as the unsteady heat transfer near the separation and reattachment points; generation of turbulent mixing layers and under-expanded jets in the interaction region, especially when they impinge on a surface. Most importantly, we need to predict and control the skin friction and heat transfer accurately, given that the usual Reynolds analogies can lead to highly inaccurate results.[1] Accurate predictions and scaling laws for interaction regions can only be achieved by understanding the fundamental physics governing the dynamics of shockwave/turbulence interactions.

In 1998, NATO established RTO Working Group 10 with a subgroup assigned to study shock-wave/turbulent-boundary layer interactions combining experiments and simulations. A great deal of insight is being gained from the efforts of this subgroup.[2,3] However, the experiments and computations were not performed at the same Reynolds number, making the resulting disagreement among experimental and computational data very difficult to diagnose. A clear demonstration of this fundamental limitation is the DNS study by Adams[4] at Mach 3 and $Re_\theta$=1,685, where the comparable experimental data were only available at much higher Reynolds numbers.

To address these issues, we are performing a joint numerical and experimental study of shockwave/turbulent boundary layer interactions (STBLI), where the simulation and experimental conditions, including Reynolds numbers, are matched as closely as possible. The DNS results were presented in Martin et al.[5] and Wu et al. [6] Here, we describe the preliminary experimental data including velocity profile surveys, surface pressure distributions, surface flow visualizations and two-dimensional flowfield imaging using Filtered Rayleigh Scattering. In addition, the numerical/experimental data comparison and analysis is described by Wu et. al.[7]

## II. Experimental Procedures, Diagnostic Techniques

### A. Facilities

The experiments in the nominal Mach 2.9 flow were done in the Princeton Gas Dynamics Laboratory Low Turbulence Variable Geometry (LTVG) facility. The tunnel consists of three major components: the high pressure air supply, test section, and ejector system (Figure 1). The high pressure air supply consists of four tanks storing 63 $m^3$ of air at pressures up to 20 MPa. The air is filtered, cooled and dried to remove particles, oil, and water before it is stored in the tanks. The test section has an overall dimension of 203 mm x 203 mm with a nominal freestream Mach number of 2.9. The freestream unit Reynolds number is $5.6 \times 10^6$ per meter resulting from typical operating conditions of $P_0$ = 73 kPa (10.6 psia) and $T_0$ = 293 K. Optical access is through one 203 mm diameter schlieren window as shown in Figure 1 and a 153 mm x 153 mm window flush-mounted in the ceiling of the test section.

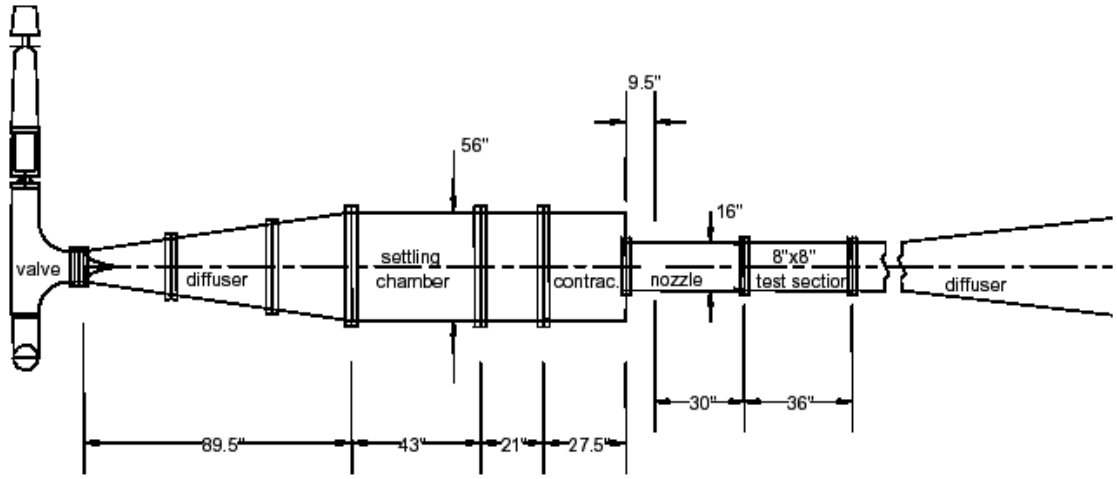


**Figure 1. Schematic drawing of the Princeton University Low Turbulence Variable Geometry wind tunnel, Mach 2.9.**

The experimental models set into the LTVG include a flat plate 584 mm long, 18.5 mm thick, spanning the entire width of the test section. The plate is centered 51 mm below the centerline of the nozzle exit with the leading edge of the plate at the exit plane of the nozzle. The plate has a single row of static pressure taps aligned in the streamwise direction. A 24º compression ramp attaches to the flat plate. The ramp is 153 mm wide and does not span the tunnel to avoid disturbances from the boundary layer on the side walls of the test section. Aerodynamic fences attached to the sides of the ramp help to prevent three-dimensional effects. It is also equipped with a single row of pressure taps aligned in the streamwise direction on the centerline. Pressure taps on the flat plate and compression ramp coincide in the spanwise direction allowing measurements of the complete mean pressure distribution. The reflected shock is generated by a 12º wedge with aerodynamic fences attached to the ceiling of the test section approximately 100 mm from the nozzle exit. Models used in the Mach 3 experiments are shown in Fig. 2.

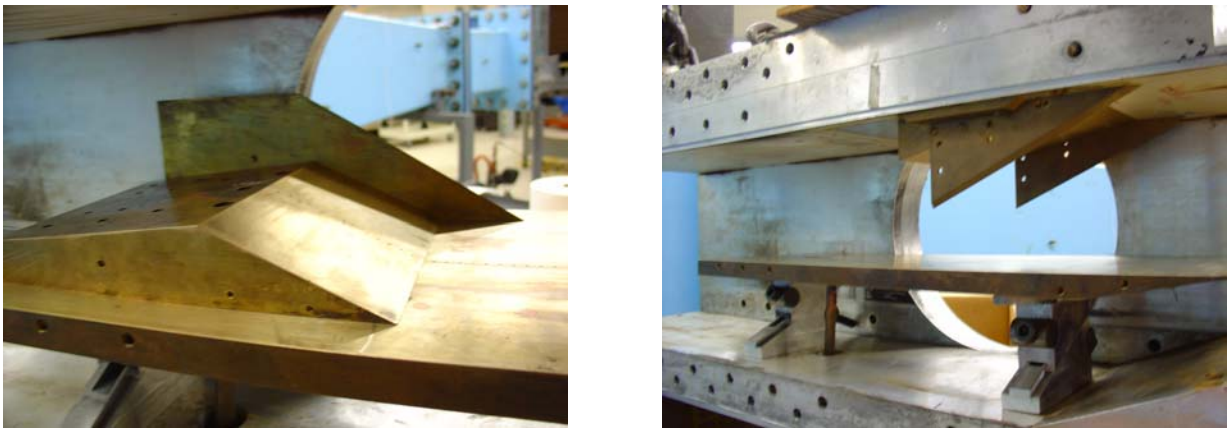

**(a)** **(b)**

**Figure 2. a) 24º compression corner model (with once aerodynamic fence removed). b) 12º reflected shock generator.**

The Mach 8 data was obtained in the Princeton Gas Dynamics Laboratory Hypersonic Boundary Layer Facility (HyperBLAF), shown in Fig. 3, with stagnation temperature of about 770K and stagnation pressure of about 1000 psi (7 MPa). The wind tunnel facility consists of four major parts: the high pressure air supply, the heating system, the hypersonic wind tunnel itself, and the ejector system which provides the low back pressure to start and maintain hypersonic flow in the test section. The high pressure air supply is the same as described for the Mach 3

experiments. The axisymmetric test section has an inner diameter of 230 mm. The unit Reynolds number in the test section can be varied from 5 x $10^6$ $m^{-1}$ to 20 x $10^6$ $m^{-1}$ by adjusting the stagnation pressure in the settling chamber (between 1.7 MPa up to 10 MPa) and the stagnation temperature (from 680K to 870K). At the diffuser inlet, the flow accelerates briefly before being compressed through a complicated shock system (there is no second throat) and then cooled to approximately ambient temperatures in the heat exchanger located upstream of the ejectors.

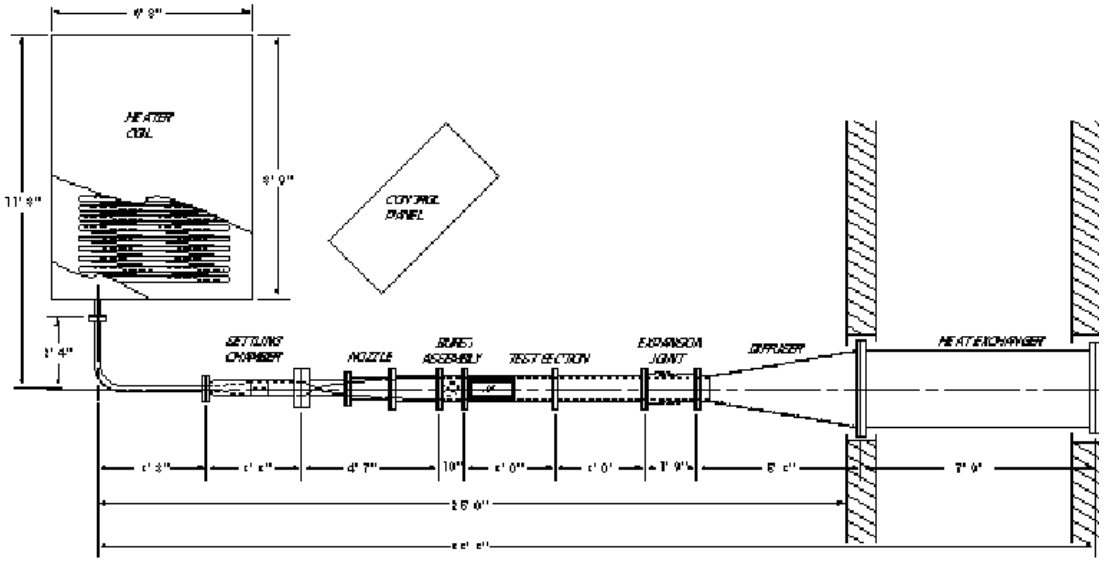


**Figure 3. Schematic of Princeton University HyperBLAF used in Mach 8 study.**

The upstream boundary layer at Mach 8 developed on a flat plate 152 mm wide and 470 mm long. The plate is supported by a central diamond-shaped support and placed in the center of the test section. The surface finish of the model is approximately 3.1 μm, considerable smaller than the viscous length scale characteristic of the flow (~76 μm). To fix the point of transition near the leading edge, a two-dimensional (cylindrical) trip was mounted at x = 58.4 mm. The trip diameter was 2.4 mm, or about 30 times the viscous length scale at that location. The shock generators used in these experiments included a full span 8º compression corner and a 10º sharp fin. These models are shown as mounted on the flat plate in Fig. 4.

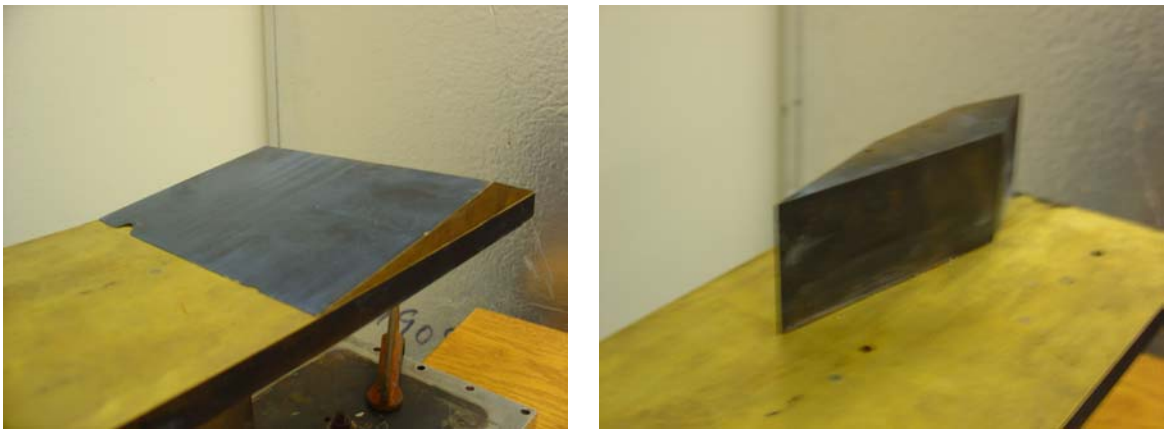

**Figure 4. a) 8º compression corner mounted on flat plate. b) 10º sharp fin three-dimensional shock generator.**

**B. Filtered Rayleigh Scattering**

Filtered Rayleigh Scattering (FRS) was used to visualize the structure of the boundary layer in all four cases. Rayleigh scattering is the scattering of light from particles that are of the order of (or less than) the wavelength of light. If the scattering particles are individual molecules, then the velocity, temperature, pressure and density can be determined from the shape and location of the intensity versus frequency curve of the scattered light. If the scatterers are not individual molecules, the static temperature and pressure information may be lost, but other useful information may still be obtained. The scatterers used in these experiments are condensed nanometer scale particles of $CO_2$, which are used to enhance the Rayleigh scattering signal. The $CO_2$ was injected upstream of the stagnation chamber in quantities ranging from 0.8% to 2.8% of the tunnel mass flux. As the air-$CO_2$ mixture cools due to expansion in the nozzle, the $CO_2$ freezes and forms nanometer-scale clusters. When the $CO_2$ clusters become entrained in the boundary layer, aerodynamic heating effects in the boundary layer causes the temperature to rise above the sublimation value and the condensate particles vaporize. The boundary layer is therefore imaged as a region of low intensity Rayleigh signal, bounded by bright regions corresponding to freestream fluid. The interface between the hot boundary layer fluid and the cold freestream flow is well-represented by the intensity of the Rayleigh scattering signal since the time scale of the sublimation is small compared to the typical time scales of the entrainment process.[8]

Figure 5a illustrates the principle of FRS. The scattering signal is Doppler-shifted by an amount proportional to the velocity of the flow. The magnitude of the shift also depends on the angles between the camera, the laser light direction vector and the predominant flow vector. The largest shift occurs when either the laser or the camera angle is parallel to the flow vector and the remaining component (either the camera angle or the laser direction) is perpendicular to the flow vector. The line shape of the scattered profile gives information on the temperature and pressure of the flow, and the total intensity of the profile is proportional to density. The magnitudes of the signals shown in Figure 5a are not to scale. Typically, the intensity of the background scattering at the frequency of the laser outweighs the intensity of the scattered signal, and without frequency discrimination, the scattered profile can be overwhelmed by the intensity of the background scattering. In Filtered Rayleigh Scattering, a molecular filter is used to provide this spectral discrimination to screen out the background scattering (see Figure 5a).

The laser used to interrogate the flow was a Spectra Physics, Q-switched, injection-seeded, frequency-doubled Nd:YAG pulsed laser with pulse energies in the 150 mJ range.[9] The laser can be tuned to wavelengths in the range from 520 nm to 550 nm, enabling the use of an iodine filter to eliminate the non-Doppler-shifted signal scattered from the wall. The duration of each pulse is 10 ns, and for single-image FRS the energy of each pulse is about 100 mJ at 532 nm. The laser was placed perpendicular to the flat plate in the streamwise direction to obtain streamwise views of the boundary layer about 310 mm downstream of the leading edge of the flat plate. (See Figure 5b).

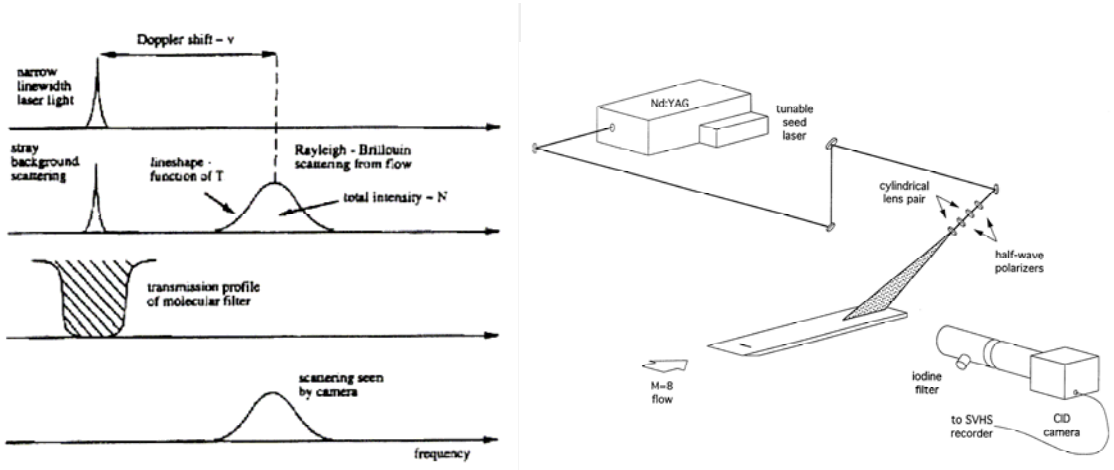


(a) (b)

**Figure 5. a) Filtered Rayleigh Scattering principles. b) Optical arrangements for FRS imaging.**

## III. Mach 2.9 Experimental Results and Discussion

### A. Undisturbed Boundary Layer

Detailed boundary layer surveys were made of the undisturbed boundary layer that formed on the surface of the flat plate. Measurements of Pitot pressure, total temperature and static pressure were made to fully characterize the scales of the undisturbed boundary layer. Measurements very near the wall could not be made due to the size of the Pitot probe. Time response was chosen over spatial resolution due to the short run times available.

The boundary-layer thickness 335 mm from the leading edge of the plate was found to be 6.7 mm ($u_e = 0.99u_\infty$). The displacement and momentum thicknesses were determined from numerical integration of the velocity profiles accounting for compressibility and were found to be $\delta^* = 2.36$ mm, and $\theta = 0.428$ mm. The Reynolds number based on momentum thickness was 2400.

The undisturbed boundary layer profile, obtained using the van Driest transformation, is shown in Fig. 6. The surveys show a well-defined turbulent profile with small logarithmic and wake regions characteristic of a low Reynolds number turbulent boundary layer. The curves were scaled using the friction velocity derived using the Clauser method. The skin friction coefficient, $C_f$, was found to be 0.00225. The deviation below the logarithmic law for $y+ < 100$ is probably due to the probe interference effects.

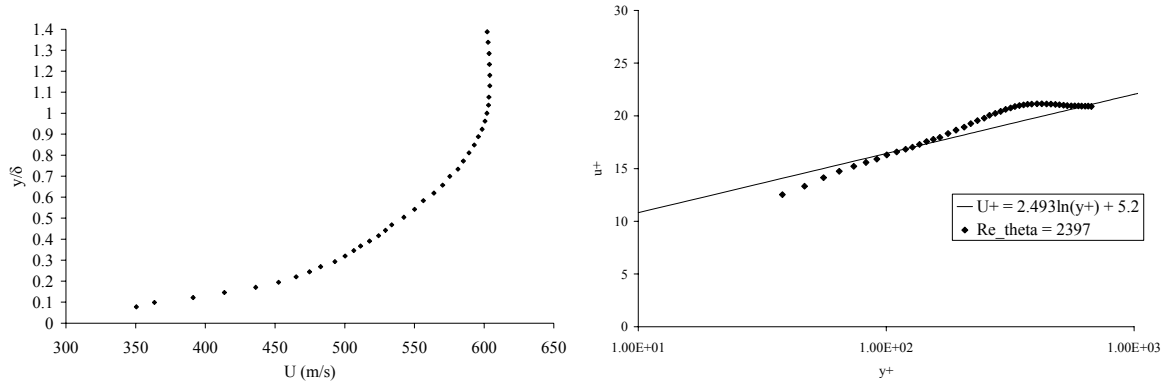


(a) (b)

**Figure 6. a) Velocity profile of Mach 2.9 undisturbed boundary layer. b) Van Driest transformed velocity profile.**

A vertical slice through the incoming boundary layer using FRS is shown in Fig. 7. Regions of cold freestream fluid appear as bright regions, and the regions of turbulent hot fluid appear dark. Deep incursions of freestream fluid can be seen in the near-wall image and turbulent bulges are seen to extend well beyond the mean boundary layer edge in the images taken in the outer layer.

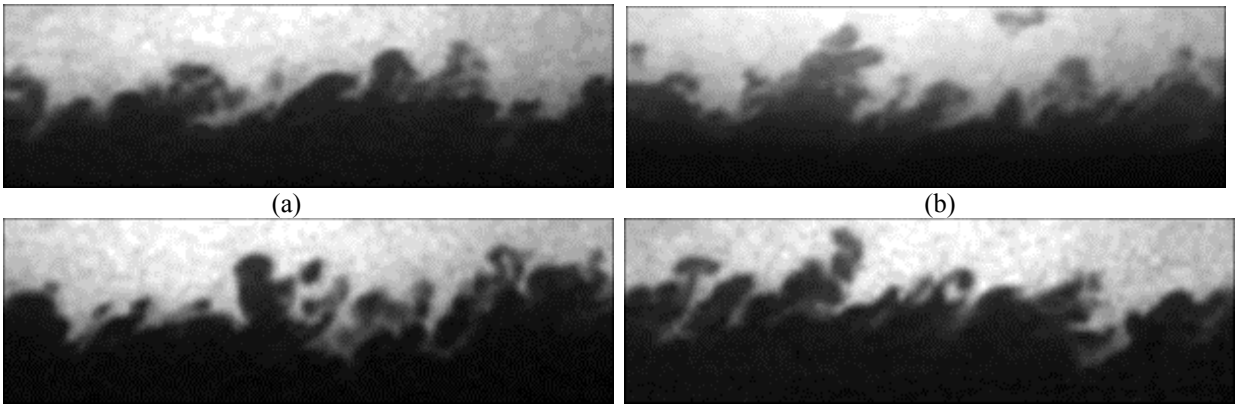

(a) (b)

(c) (d)

**Figure 7. Instantaneous side view FRS images (uncorrelated) of the Mach 2.9 undisturbed boundary layer. Images are $1.5\delta_0$ x $5\delta_0$. The bottom edge of each image corresponds to the plate location.**

From the FRS images, we can investigate the intermittency, mean structure angles and mean length scales. The intermittency was determined by applying a simple threshold to the grayscale values. The interface between turbulent and non-turbulent fluid is very apparent, so the images are very insensitive to the threshold level. The images are 8 bit grayscale and a grayscale value of 75 was selected that accurately exhibits the interface, as seen in Figure 8a. Analysis over a total distance of 700δ from 139 images result in the intermittency profile shown in Figure 8b. The results show a slightly steeper profile than that observed in incompressible flow, which may indicate more the different techniques used to measure the intermittency, rather than actual differences in flow structure. The effect of varying the threshold level by ±10 is shown in Fig. 8b. The loss of signal at about half the boundary layer height discovered in the correlation analysis (described below), gives a possible explanation why the proportion of turbulent fluid is higher than expected. Within experimental error, there is no discernible difference between this supersonic boundary layer and the profile derived for subsonic boundary layers by Klebanoff.[10]

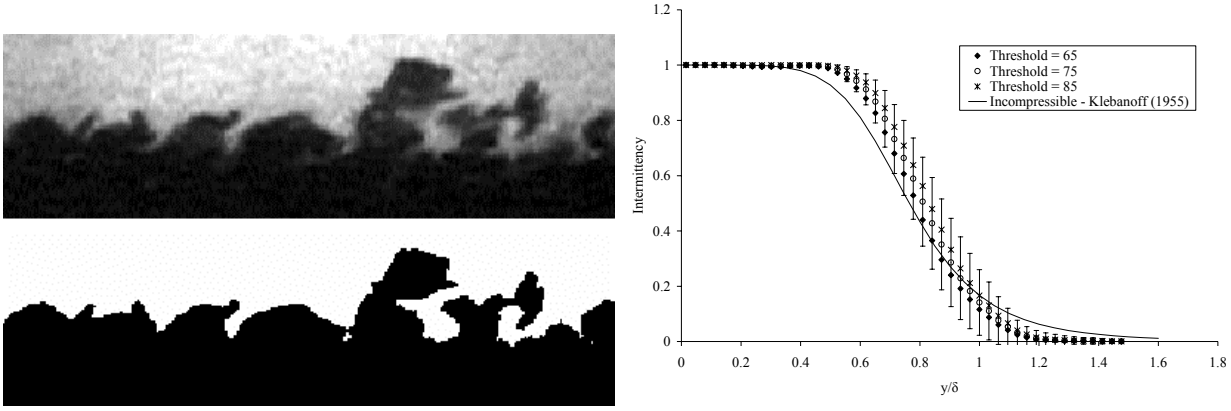


(a) (b)

**Figure 8. a) Application of threshold technique to Mach 2.9 undisturbed boundary layer. b) Intermittency function**

Correlations were used to determine the mean structure angles. The correlation coefficient was determined from the following equation:

$$C_{i,j} = \frac{\sum_{n=1}^{k}\left(X^{k}_{i,j} - \overline{X}_{i,j}\right)\left(X^{k}_{i_0,j_0} - \overline{X}_{i_0,j_0}\right)}{\sqrt{\sum_{n=1}^{k}\left(X^{k}_{i,j} - \overline{X}_{i,j}\right)^2}\sqrt{\sum_{n=1}^{k}\left(X^{k}_{i_0,j} - \overline{X}_{i_0,j_0}\right)^2}} \qquad (1)$$

where $X^k$ is a random variable representing the grayvalue of frame *k, i* and *j* are pixel coordinates, 0 denotes a reference coordinate, and $\overline{X}$ is the ensemble average. Equation 1 is derived directly using the estimators for the variance and covariance of a random sample. An ensemble of one hundred randomly chosen images (1δ x 1.2δ in size) of the incoming boundary layer was used to make the correlations. The reference points were fixed in the *i* direction (spanwise) at the center of each image. The *j* direction (wall normal) was varied at progressively higher y/δ. The correlation coefficients ranged from -0.3 to 1.0. Thresholding was applied to the coefficients to simplify the images for analysis by grouping the coefficients into one of 7 ranges: -0.3 to -0.1, -0.1 to 0.1, 0.1 to 0.3, 0.3 to 0.5, 0.5 to 0.7, 0.7 to 0.9, and 0.9 to 1.0. An example of the resulting contoured images is shown in Fig. 9. The lower edge of these images corresponds to the location of the flat plate. Ellipses were fitted to the contour levels of 0.6, 0.7, 0.8 and 0.9. The angle of the major axis of the ellipses with respect to the flat plate for each of these contours was measured and averaged to determine the mean structure angle through the boundary layer. The mean structure angles for y/δ > 0.5 are shown in Fig. 10. The results show a range of structure angles from 45º to 60º. The structure angle increases with distance from the wall. Accurate measurements for y/δ < 0.5 were not possible due to the loss of signal strength in the lower half of the boundary layer. The data compares favorably with the hot-wire data of Spina et al. ( M = 2.9, $Re_0 \approx 80{,}000$).[11] The structure angles found in this study lie on the lower extent of Spina's data, suggesting a possible Reynolds number dependence. However, no conclusion regarding any Reynolds number dependence can be drawn here due to uncertainties of all the methods.

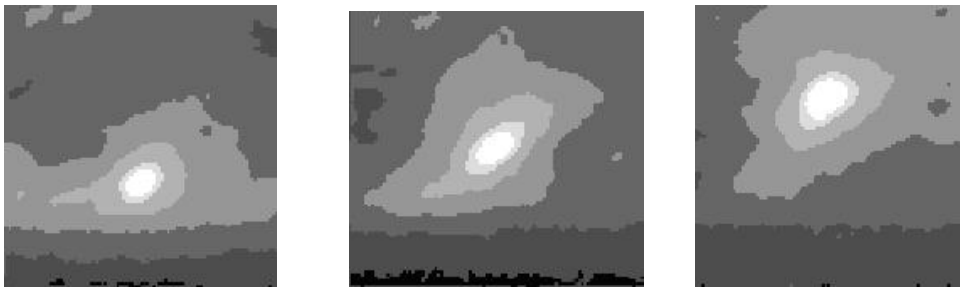

**Figure 9. Mach 2.9 undisturbed boundary layer correlation contour images at y/δ = 0.55, 0.75, and 1.0 from left to right.**

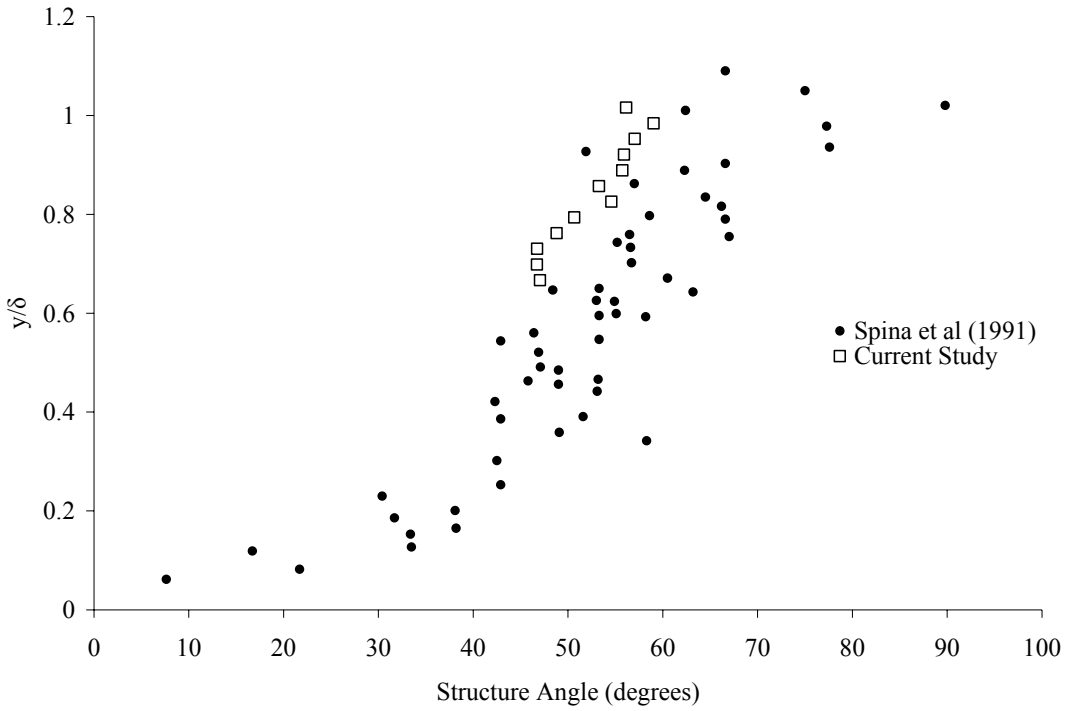


**Figure 10. Mach 2.9 undisturbed boundary layer mean structure angle calculated from FRS correlations**

**B. 24º Compression Corner Interaction**

The 24º compression corner interaction was studied using boundary layer surveys and FRS images. The presence of separation was indicated by the formation of the shock well ahead of the physical corner location in FRS images.

The boundary layer profiles for the 24º compression corner are shown in Fig. 11a and transformed according to Van Driest in Fig. 11b. The profiles are seen to rapidly fill out with distance up the ramp, most likely due to enhanced turbulent mixing from the formation of large scale eddies.[12] The decrease in the streamwise velocity in the outer parts of the boundary layer is also seen in Fig. 11a. This suggests that the flow was still turning and decelerating in the final stages of the compression process.

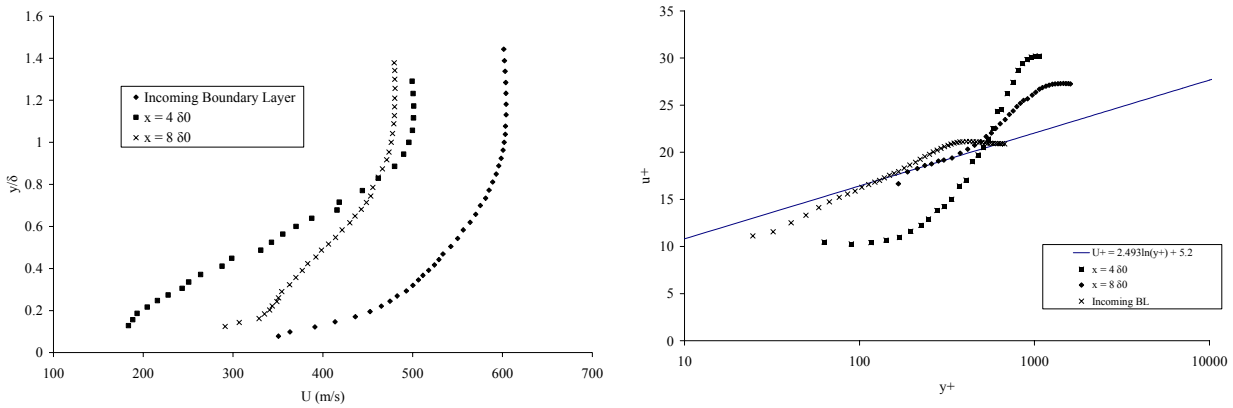


(a) (b)

**Figure 11. a) Velocity profiles through Mach 2.9 24º compression corner interaction. b) Velocity profiles transformed according to van Driest.**

The results of the FRS imaging of the 24º compression corner interaction are shown in Fig. 12. The temperature behind the shock rises to a level greater than the sublimation temperature of the carbon dioxide so that there is a rapid loss of signal behind the shock and subsequently loss of the ability to further analyze the downstream boundary layer. However, estimates of the separation length, $X_s$, which is the distance from the corner location, can be made by examining the images for the location of the shock foot. The location was found by extrapolating the shock with a straight line to the flat plate location. This analysis found the separation length to be $2\delta_0 \pm 7\%$ upstream of the corner location from 50 images. These estimates are crude since the images don't reveal the shock location throughout the boundary layer. Curvature of the shockwave due to Mach number variation cannot be accounted for, so these estimates are expected to overestimate the separation length. A more precise method for determining the extent of the separated region is currently underway using surface pressure measurements and surface flow visualization.

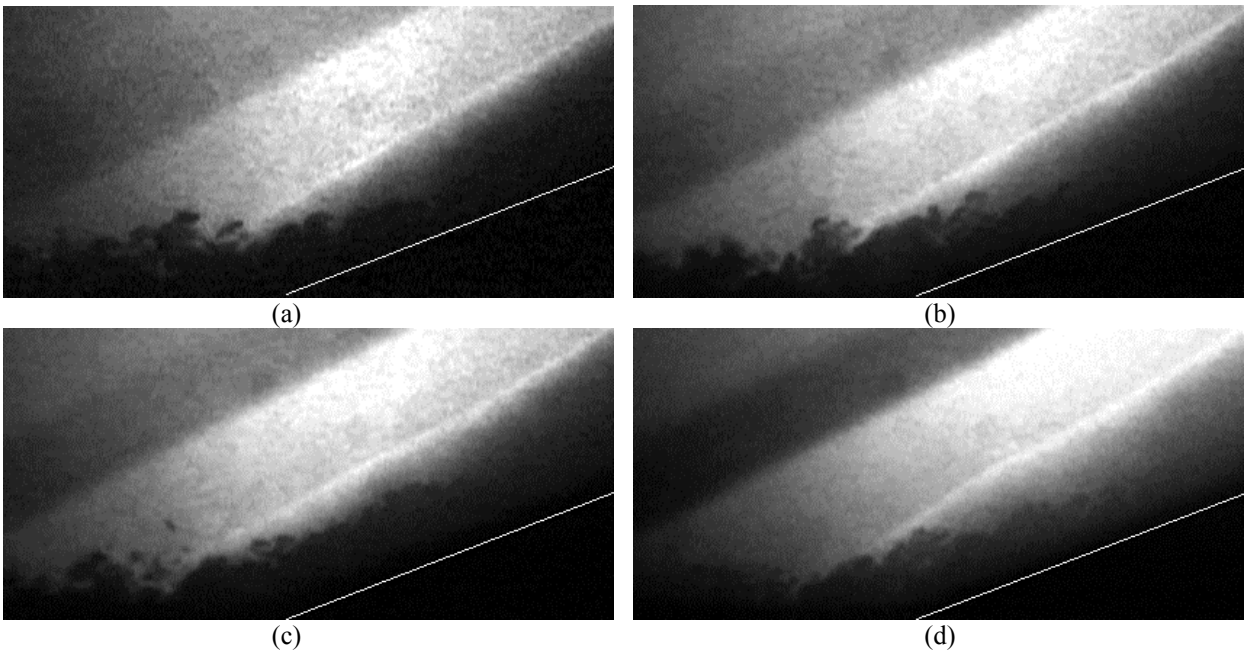

(a) (b)

(c) (d)

**Figure 12. Instantaneous FRS images (uncorrelated) of Mach 2.9 24º compression corner interaction. The white line indicates the ramp location. Images are $3.3\delta_0$ x $7\delta_0$. Upstream wall location is the bottom edge of each image.**

FRS images were used to examine the change in the intermittency and mean structure angle through a small part of the interaction. Due to the loss of signal behind the shock, only the boundary layer immediately downstream of the shock could be examined. This corresponds to the region of separated flow. The results of the intermittency function and mean structure angle, determined as described for the incoming boundary layer, are shown in Fig 13.

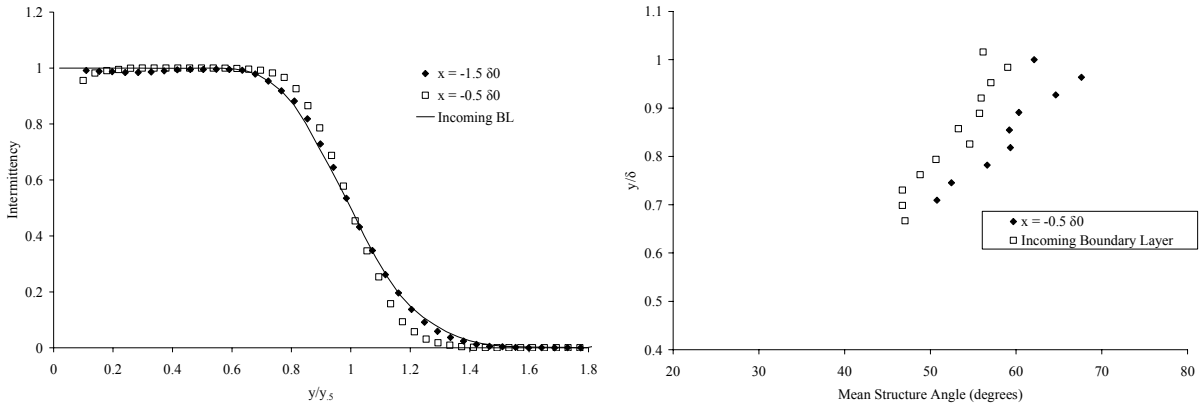


(a) (b)

**Figure 13. a) Intermittency function through Mach 2.9 24º compression interaction. b) Mean structure angles through boundary layer.**

Figure 13a shows the intermittency through the first part of the interaction. The intermittency function provides information about the proportion of turbulent fluid present at a given height in the boundary layer. The wall normal position is normalized by the position where the intermittency reaches 50%. The absolute position where this occurred increased by only a few percent through the part of the interaction studied. For the incoming boundary layer, this occurred at $y = 0.8\delta_0$ and increased to $0.85\delta_0$ at $x = -0.50\delta_0$. The mean structure angle is seen to exhibit similar features as the incoming boundary layer, with increasing structure angle with height. The wall normal position is normalized by the incoming boundary layer height. Figure 13b indicates that the large-scale structures in the outer part of the layer are inclined at a greater angle relative to the flat plate. These measurements were made relative to the plate, so the flow is likely to have begun to turn at the location studied. At this point, the flow would have made the initial turn through the separation shock. This would cause the angle of the structures to appear to have increased. However, the turning of the mean flow would be small at this point, so the structure angle has likely increased with respect to the mean flow direction.

### C. Reflected Shock Interaction

The 12º reflected shock interaction was studied using boundary layer surveys and FRS images. The presence of separation was indicated in FRS images by the formation of the reflected shock well ahead of the point where the incident shock would meet the surface if the fluid were inviscid. This reflected shock intersected the incident shock well outside the boundary layer.

Boundary layer profiles of the interaction are shown in Fig. 14. The flow field was first imaged using FRS to specify the location of the shock impingement. The mean position of the intersection of the impinging shock and separation shock was found to be a good reference point for the x-location. It is clear that the flow at $2\delta_0$ behind the intersection is highly separated with a large extent of the velocity profile exhibiting flow reversal. The point where the velocity equals zero is a good indicator of the height of the separation bubble, in this case about 6 mm at the surveyed location. At $x = 8\delta_0$, the flow has reattached, but the velocity profile has wake-like properties similar to the 24º compression ramp case.

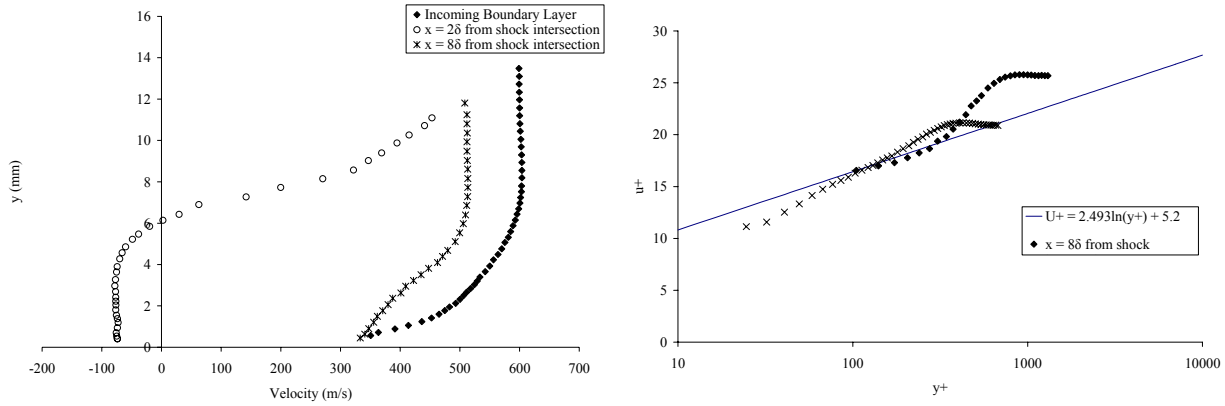


(a) (b)

**Figure 14. a) Velocity profiles through incident shock interaction. b) Van Driest transformed velocity profiles.**

Vertical slices through the reflected shock interaction are shown in Fig. 15. Similar to the compression corner images, the signal degrades rapidly behind the shock due to the associated temperature rise beyond the carbon dioxide sublimation level. Using the conventions shown in Fig. 15a, the separation shock (C2) is seen to begin well ahead of where the incident shock (C1) would impinge on the flat plate in an inviscid flow. The boundary layer thickness significantly increases through the interaction as the flow turned over the separation bubble.

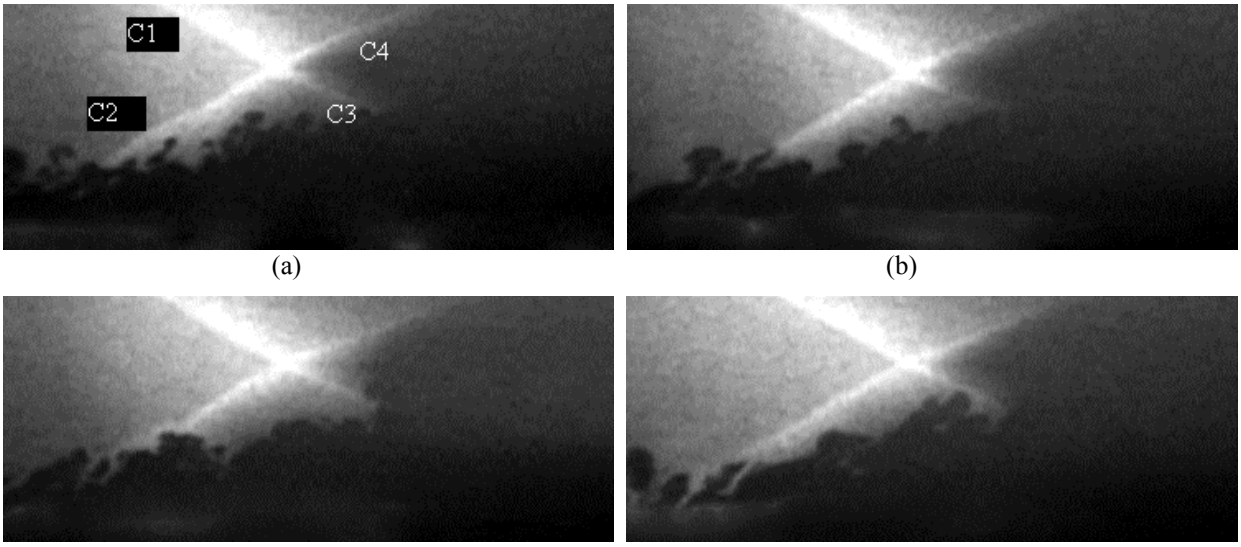


(a) (b)

(c) (d)

**Figure 15. Instantaneous FRS images (uncorrelated) of reflected shock interaction at Mach 2.9. Images are $2.3\delta_0$ x $6\delta_0$.**

FRS images were used to examine the intermittency through the initial part of the interaction. The loss of signal strength through the shock system prevents analysis further downstream. Fig. 16 was produced using the method described above. The intermittency profile exhibits the same behavior as found in the compression corner. The profile becomes steeper through the initial part of the interaction at x = -1.5 $\delta_0$. The profiles further downstream showed no significant change. The location where the profile reached 50% ($y_{0.5}$) increased rapidly through the interaction. The $y_{0.5}$ location was seen to rise by 4%, 33% and 59%, respectively for the three streamwise positions examined in Fig. 16. This quantifies the significant boundary layer thickness growth seen in the FRS images.

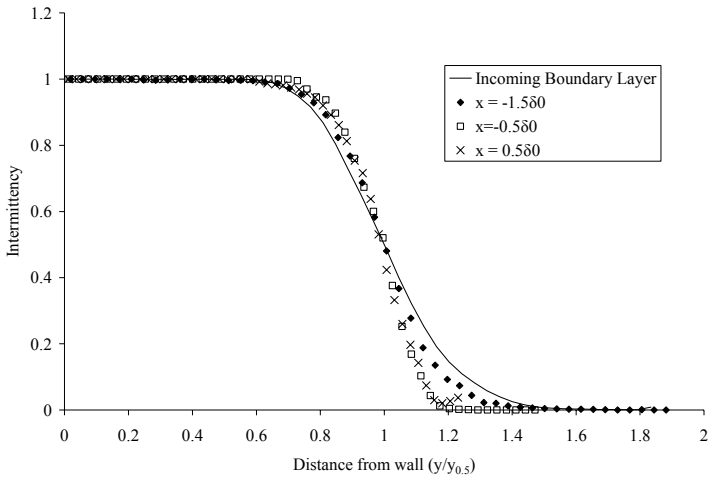


**Figure 16. Intermittency profile at 4 streamwise positions in reflected shock interaction**

## IV. Mach 8 Experimental Results and Discussion

### A. Undisturbed Boundary Layer

The undisturbed turbulent boundary on a flat plate at Mach 8 was studied extensively by Baumgartner.[13] An independent survey of the boundary layer was not undertaken in this study. The test conditions ($p_0$=1000psia, $T_0$=810 K) used by Baumgartner were replicated so that the boundary layer characteristics were approximately the same as his results. He found the boundary-layer thickness 360 mm from the leading edge of the plate to be 11.5 mm ($u_e = 0.99u_\infty$). The displacement and momentum thicknesses were determined from numerical integration of the velocity profiles accounting for compressibility and were found to be $\delta^* = 5.9$ mm, and $\theta = 0.2$ mm. The Reynolds number based on momentum thickness was 3500.

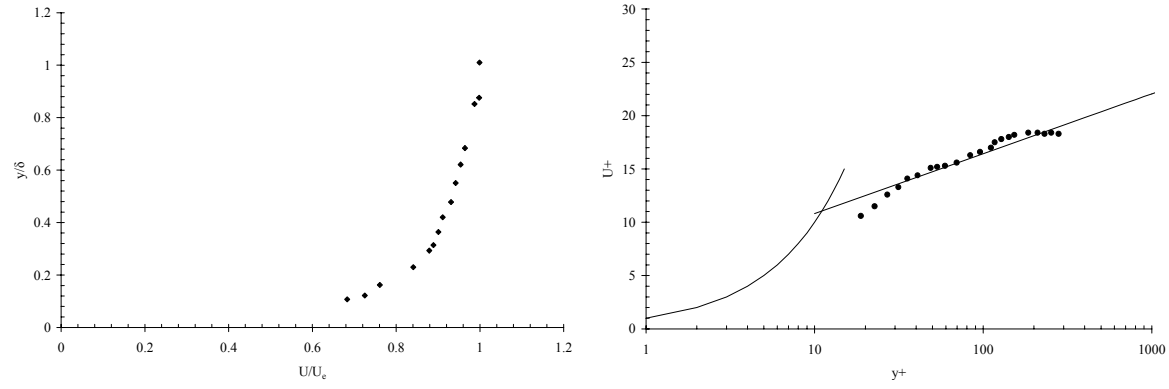


(a) (b)

**Figure 17. a) Velocity profile of Mach 8 undisturbed boundary layer. b) Van Driest transformed velocity profile.**

Further details of the undisturbed boundary layer were obtained using the Van-Driest transformation, shown in Fig. 17. The surveys show a well-defined turbulent profile with small logarithmic and wake regions characteristic of a low Reynolds number turbulent boundary layer. The curves were scaled using the friction velocity derived using the Clauser method. The skin friction coefficient, $C_f$, was found to be 0.00072.

FRS images of the undisturbed boundary layer are shown in Fig. 18. The same methods as described for the Mach 3 boundary layer were used by Baumgartner to investigate the intermittency, mean structure angles, and mean structure size. The results of these analyses are shown in Fig. 19.

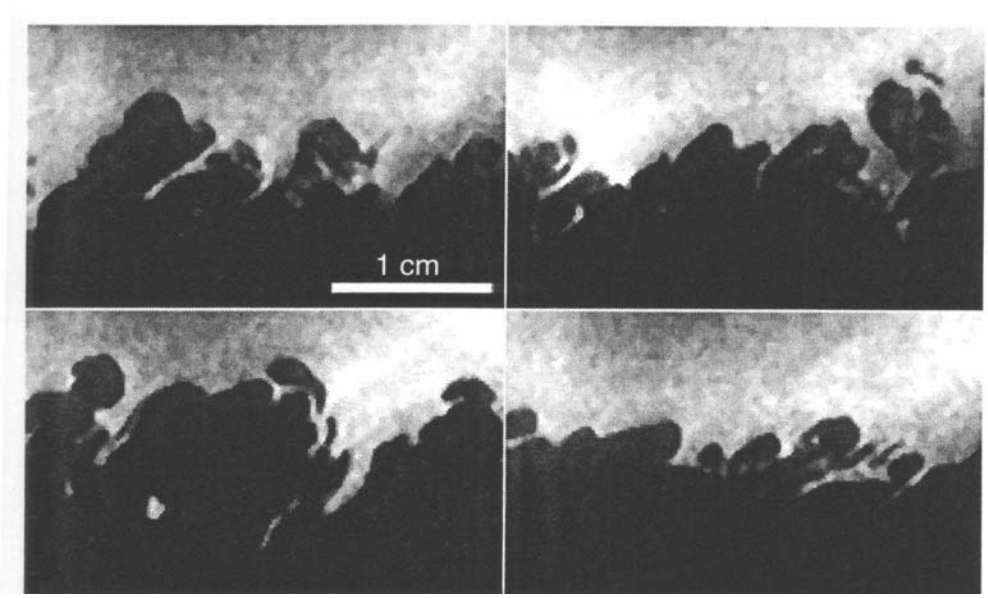


**Figure 18. FRS images (uncorrelated) of Mach 8 undisturbed boundary layer. Images are 1.5 $\delta_0$ x 2.5 $\delta_0$. Wall location corresponds to bottom edge of image.**

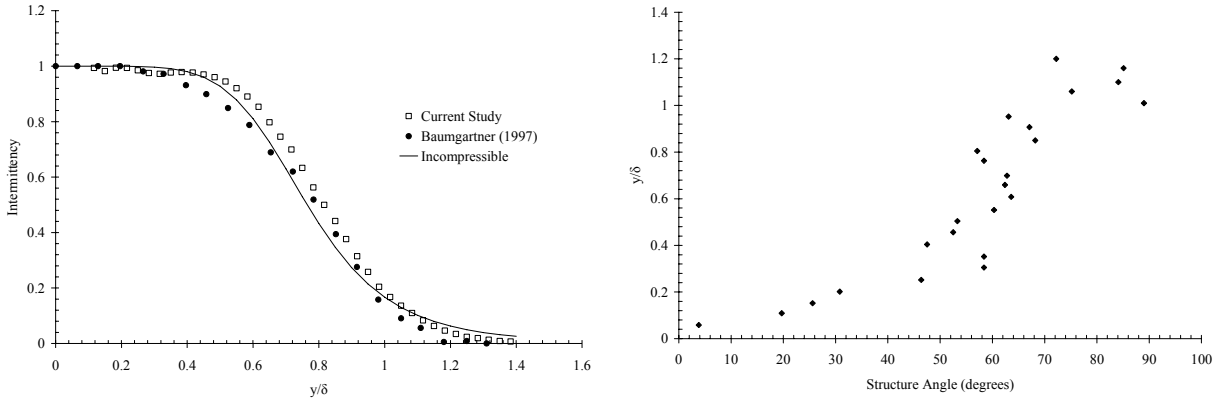


(a) (b)

**Figure 19. a) Intermittency of Mach 8 undisturbed turbulent boundary layer. (b) Mean structure angles through boundary layer.**

### B. 8º Compression Corner Interaction

The 8º compression corner was examined using surface flow visualizations and FRS. The surface flow visualization was done using a mixture of 1,000 centistokes Dow Corning 200 silicone fluid and titanium dioxide powder. The resulting white mixture was highly visible against the black painted background of all models. Tunnel shutdown proved to significantly alter the flowfield structure, so a video-camera was employed to record the oil flow. Subsequently, individual frames were grabbed from the video and used for analysis. One image of the surface flow pattern for this flowfield is shown in Fig. 20. The image shows that the flow has remained attached as the surface skin-friction lines are continuous through the corner location and no distinct separation line is present. Analysis of the video showed that the oil flow slowed near the corner and then accelerated up the ramp with no flow reversal. This behavior reflects the wall shear stress decreasing as the flow approaches the corner, and then increasing downstream of the corner. The oil flow visualization also shows the highly two-dimensional flowfield about $10\delta_0$ wide along the centerline of the flat plate in the streamwise direction. Three-dimensional effects are only present near the sides of the wedge where disturbances from tunnel walls and the edge of the plate start to appear.

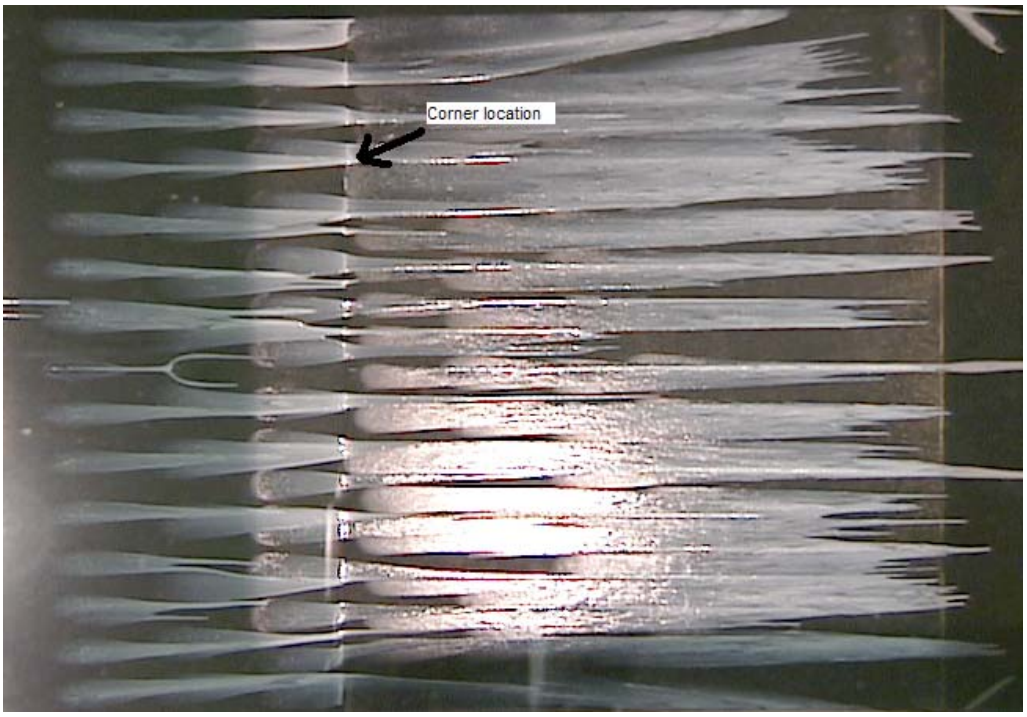


**Figure 20. Surface oil flow visualization the Mach 8 8º compression corner interaction**

FRS images of the 8º compression corner were taken in two locations. The first location showed the incoming boundary layer and the first half of the ramp. The second location ignored the incoming boundary layer and concentrated on the boundary layer on the ramp only. These images are seen in Figs. 21 and 22. The shockwave was deeply immersed in the boundary layer and highly distorted by passing large scale structures. The distortion of the shockwave is still prominent several boundary layer thicknesses downstream of the corner. There is no significant boundary layer growth and no indication of separation.

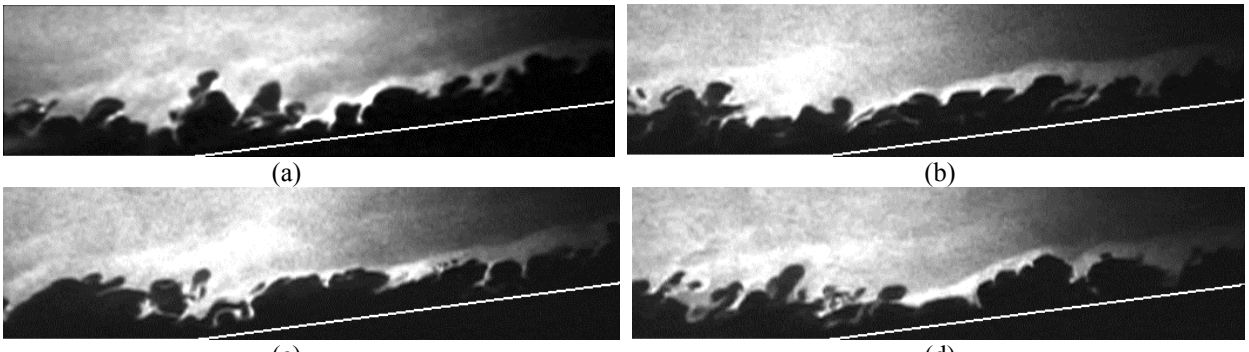


**Figure 21. Instantaneous FRS images (uncorrelated) of the Mach 8 8º compression corner interaction. Images are $1.7\delta_0$ x $6\delta_0$. The corner location is the intersection of the white line with the bottom edge of the image which is the wall location.**

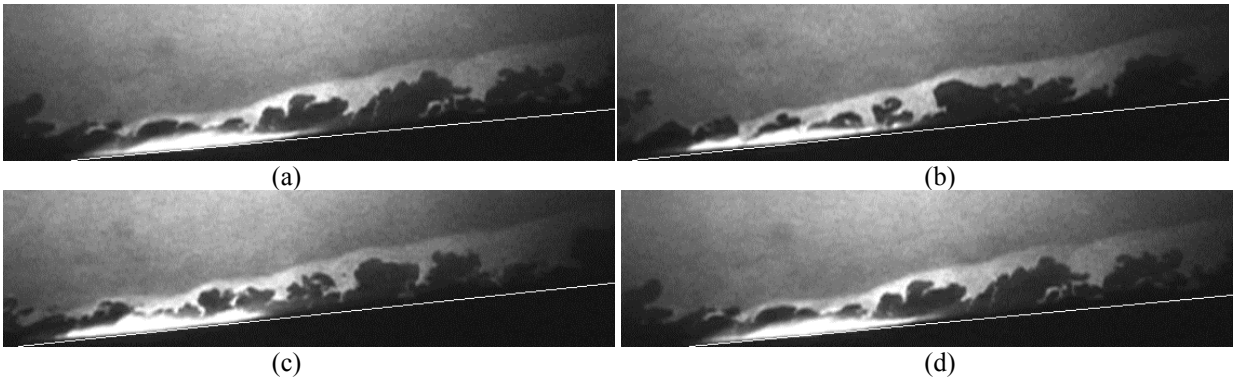


**Figure 22. Instantaneous FRS images (uncorrelated) of the Mach 8 8º compression corner interaction (further downstream). Images are $1.8\delta_0$ x $6.5\delta_0$. The bright flares on the plate surface are bright spots in the laser sheet.**

### C. 10º Sharp Fin Interaction

Oil flow visualizations of the skin-friction lines of the 10º sharp fin interaction were obtained with the same silicon oil titanium dioxide mixture used for the compression ramp study. The surface streamlines on the flat plate are shown in Fig. 23. A schematic of the flowfield is included as Fig. 24, which highlights the features of the surface flow: upstream influence (U), inviscid shock surface trace (0), primary separation ($S_1$) and primary attachment (A). Both the primary and secondary separation lines are evident. The reattachment line is not as readily apparent, but is believed to lie just off the surface of the fin. Figure 25 indicates that the surface flow is quasi-conical. With the exception of the inception region (i.e., near the fin leading edge), surface lines can be traced upstream to a common point. The upstream influence line, primary separation line and inviscid shock trace can be traced back to a virtual origin, which is located at x = -39 mm ($-3.3\delta_0$) and z = -11 mm ($-0.97\delta_0$) in the coordinates defined in Fig. 24 where the fin leading edge is the origin.[14] The inception length, defined as the linear distance from the fin leading edge to the beginning of the conical region, was found using the following technique. A straight line was drawn along the primary separation line. The location where this line diverged from the actual separation line was defined as the end of the inception region. Although there is some subjectivity in defining these locations and angles, more sophisticated methods have produced results that do not substantially differ from visual results.[14] The inception length found for this configuration was $L_i$ = 36 mm ($3.1\delta_0$). This estimate must be taken in the context of its subjectivity and might be more useful as a qualitative, rather than quantitative result. These results agree well with the data of Ref. 15 for a sharp fin at Mach 5.

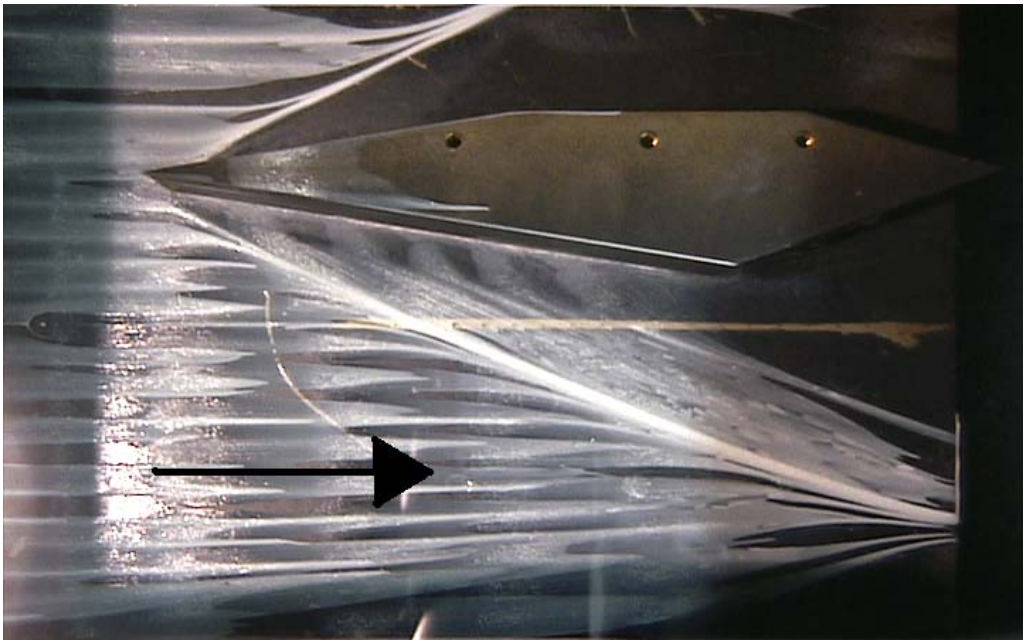

**Figure 23. Surface oil flow visualization 10º Sharp Fin interaction at Mach 8**

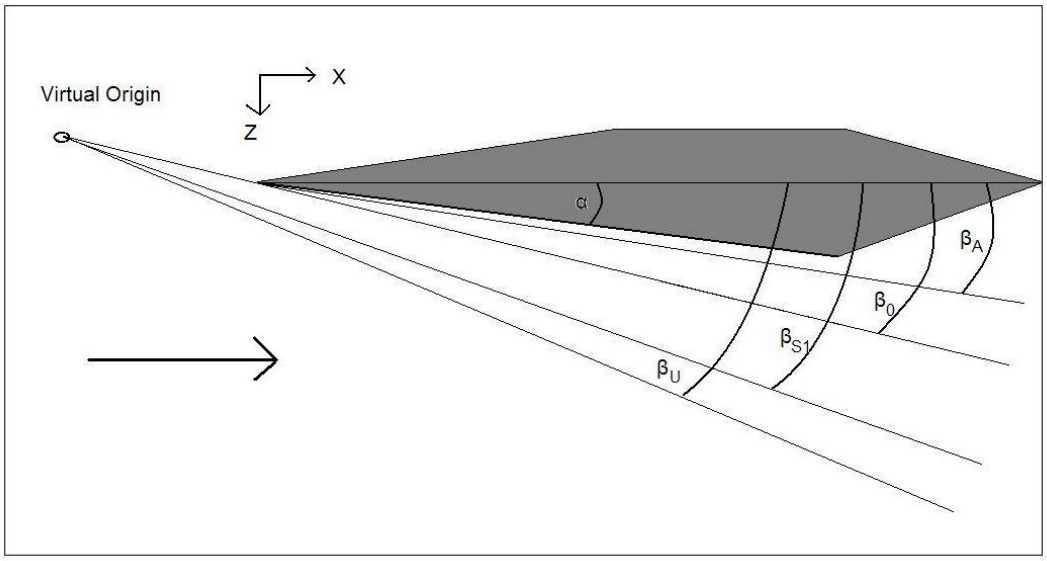


**Figure 24. Schematic of oil flow visualization**

FRS images were used to visualize the interaction. The quasiconical symmetry of the interaction suggests that the natural coordinate system to be used would be a spherical coordinate frame centered on the virtual origin. This suggests that the most pertinent visual images should be made in planar sheets normal to the inviscid oblique shock generated by the fin. However, the highly swept interaction ($\beta_0 \approx 16º$) at the high Mach number caused this type of imaging to be very difficult due to the optical access limitation inherent in the hypersonic wind tunnel. Filtered Rayleigh scattering images were taken normal to the flat plate parallel to the freestream ahead of the shock. Images were taken at two spanwise locations to establish the growth of the quasiconical interaction. The first location images, shown in Fig 25, were taken at z = 21 mm (1.8 $\delta_0$) from the leading edge of the fin. The inviscid shock is readily apparent in these images with the separation shock visible about $3\delta_0$ ahead of the inviscid shock location, in good agreement with the location found from the separation line found in flow visualization images. The point of shock bifurcation is clearly seen. The turning of the flow is evident downstream of the inviscid shock as the

boundary layer appears to be breaking up, but this is simply a result of the large structures in the boundary layer having a component of the mean velocity coming out of the image. The significant boundary layer growth is also evident; however the separation bubble appears dark for reasons discussed earlier with regard to the flow seeding mechanism.

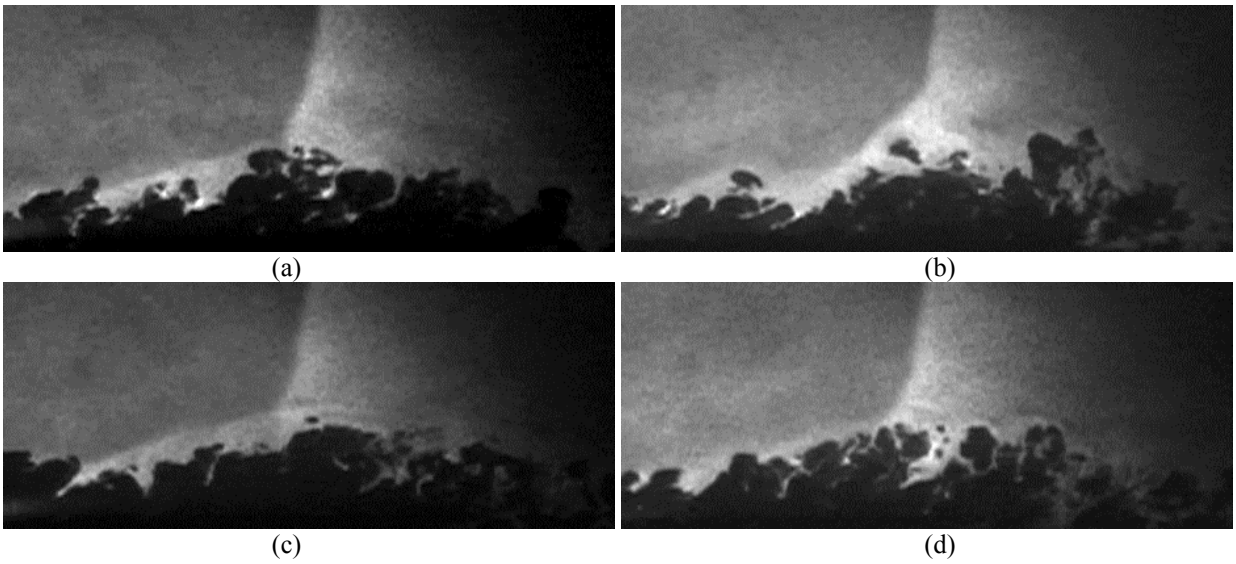


**Figure 25. Instantaneous FRS images (uncorrelated) at z = 21 mm (1.9 $\delta_0$) from 10º sharp fin. Images are $3\delta_0$ x $6\delta_0$. The wall location coincides with the bottom of each image.**

Figure 26 shows the FRS images taken at z = 32 mm from the fin leading edge. The inviscid shock location is not nearly as evident as the closer location. Reasons for this are unknown, but its location is evident by the abrupt change in contrast in the freestream and the triangular shape of the shock bifurcation location. The separation shock is seen extending upstream about $4\delta_0$ from the inviscid shock location in excellent agreement with measurements from flow visualization.

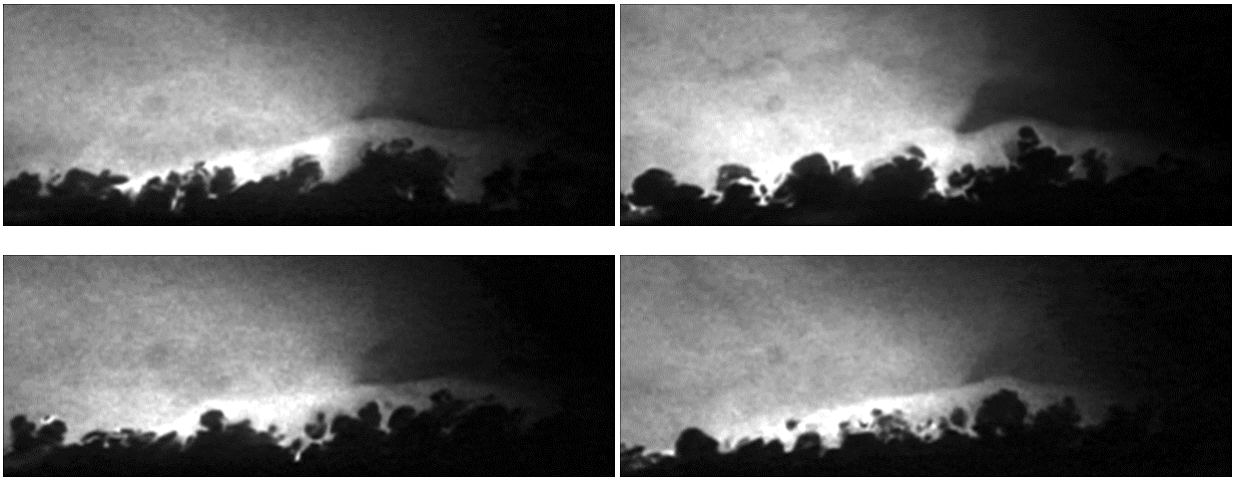

**Figure 26. Instantaneous FRS images (uncorrelated) at z = 32 mm (2.7 $\delta_0$) from 10º sharp fin. Images are $2.9\delta_0$ x $7.1\delta_0$.**

## V. Conclusions

The flowfield structure of four shock/turbulent boundary layer interactions has been studied using mean flow surveys, surface flow visualization, and Filtered Rayleigh Scattering. The results of this study serve as the foundation for the compilation of a database of experimental results at flow conditions accessible to numerical simulations. In depth examinations of each of the flowfields studied here, including examination of the turbulent flow field, will strengthen the comparisons between numerical and experimental results.

## Acknowledgements

This work was sponsored by the Air Force Office of Scientific Research, USAF, under grant # F49620-02-1-0361.

## References

1. Evans, T., and Smits, A.J. Measurements of the Mean Heat Transfer in a Shock Wave Turbulent Boundary Layer Interaction. *Experimental Thermal and Fluid Science*, **12**, 87-97 (1996).
2. Knight, D. RTO WG 10: Test Cases for CFD Validation of Hypersonic Flight. AIAA Paper No. 2002-0433 (2002).
3. Knight, D., Tan, H., Panaras, A., and Zheltovodov, A. RTO WG 10: CFD Validation of Shock Wave Turbulent Boundary Layer Interactions. AIAA Paper No. 2002-0437 (2002).
4. Adams, N.A. "Direct simulation of the turbulent boundary layer along a compression ramp at M=3 and Reθ=1685,'' Journal of Fluid Mechanics, 420, 4 (2000).
5. Martin, M.P., S. Xu, and M. Wu, ``Preliminary Work on DNS and LES of STBLI,'' AIAA-2003-3464, June 2003.
6. Wu, M., and Martin, M.P., "Direct Numerical Simulation of Shockwave/Turbulent Boundary Layer Interaction,", AIAA Paper No. 2004-2145, *34th AIAA Fluid Dynamics Conference and Exhibit*, Portland, OR. June 2004.
7. Wu, M., and Martin, M.P., "Analysis of Shockwave/Turbulent Boundary Layer Interaction Using DNS and Experimental", AIAA Paper No. 2005-0310, *43th AIAA Aerospace Sciences Meeting and Exhibit*, Reno, NV, January 2005.
8. Erbland, P.J. Filtered Rayleigh Scattering and Homogeneous Nucleation of $CO_2$ in Supersonic Flows. PhD Thesis, Princeton University (2000).
9. Miles, R.B., J.N. Forkey and W.R. Lempert, "Filtered Rayleigh Scattering Measurements in Supersonic/Hypersonic Facilities," AIAA Paper 92-3894, *17th Aerospace Ground Testing Conference,* Nashville, TN. July 1992.
10. Klebanoff, P.S., "Characterisistics of Turbulence in a Boundary Layer with Zero Pressure Gradient," NACA Report 1247, 1955.
11. Spina, E.F. Donovan, J.F., and Smits, A.J. "On the Structure of High-Reynolds-Number Supersonic Turbulent Boundary Layers," *Journal of Fluid Mechanics,* 222: 293-327, 1991.
12. Kuntz, D.W., Amatucci, V.A., and Addy, A.L., "Turbulent Boundary-Layer Properties Downstream of the Shock-Wave/Boundary-Layer Interaction," *AIAA Journal*, Vol. 25, No. 5, 1986, pp.668-675.
13. Baumgartner, M. L. Turbulence Structure in a Hypersonic Boundary Layer. PhD Thesis, Princeton University (1997).
14. Settles, G.S., and Dolling, D.S. "Swept Shock/Boundary-Layer Interactions – Tutorial and Update," AIAA Paper No. 90-0375, *28th Aerospace Sciences Meeting,* Reno, NV. January 1990.
15. Rodi, P.E., and Dolling, D.S., "An Experimental/Computational Study of Sharp Fin Induced Shock Wave/Turbulent Boundary Layer Interactions at Mach 5: Experimental Results," AIAA 92-0749, *30th Aerospace Sciences Meeting and Exhibit,* Reno, NV, January 1992.